

ADVANCED MATERIALS

Supporting Information

for *Adv. Mater.*, DOI: 10.1002/adma.202208920

Direct Visualization of Localized Vibrations at Complex
Grain Boundaries

Eric R. Hoglund, De-Liang Bao, Andrew O'Hara,
Thomas W. Pfeifer, Md Shafkat Bin Hoque, Sara
Makarem, James M. Howe, Sokrates T. Pantelides,*
Patrick E. Hopkins,* and Jordan A. Hachtel**

Supporting Information: Figure Captions

Figure S1. **Drift-correction of Aberration-corrected HAADF Image in the 10° GB.** Images acquired at (a) 0° and (b) 90° scan rotations with inset fast-Fourier-transforms showing a skewed reciprocal lattice. The image in (b) was rotated for better comparison with (a). (c) Image after drift correction. 3

Figure S2. **Atom Positions in Four Drift-corrected HAADF Images.** (a-d) Drift-corrected HAADF images showing the (green) Sr, (cyan) Ti, and (red) core sublattices. 4

Figure S3. **SVD scree plots.** Scree plots for (a) 0-50 and (b) 50-250 components. (a) Shows the first elbow at component 4 and (b) shows the second elbow at component 110. 5

Figure S4. **SVD of TiO core-loss spectrum image of the 10° GB.** (a-c) Ti- L_{23} edge (a) averaged from each region, and from individual points in the (b) grain and (c) GB. (d-f) O- K edge (d) averaged from each region, and from individual points in the (e) grain and (f) GB. The colors of the lines correspond to the order of background subtraction and decomposition and the number of components, as indicated in the legend. In (a,c) the grain (solid) and dislocation-core (dot-dashed) signals overlap for each region because of the large number of averaged pixels. 6

Figure S5. **NMF abundance map distributions.** Histograms of NMF abundance maps in Figure 4(a,b). Distributions in the grain (solid) are from x-positions >1.5 nm from the GB center position. Distributions at the GB (dashed) are from -1.5 to 1.5 nm from the GB center position. . 9

Figure S6. **Off-Axis EELS Collection Geometry and Resolution.** (a) Schematic for high spatial resolution vibrational EELS off-axis collection geometry. With a convergence semiangle of 30 mrad and a collection semiangle of 25 mrad, the beam is deflected by ~18 mrad such that the majority of the collection aperture accepts only high angle scattering events. This reduces the delocalized dipole scattering dominant in the bright field disk and emphasizes the localized impact scattering dominant at the higher angles to provide a high spatial resolution signal.^[7,8] (b) Two-dimension display of the averaged hyperspectral dataset shown for vibrational EELS in the main text. Here, the x-axis represents energy loss (the dispersive axis of the spectrometer) and the y-axis represents the effective scattering angle (the non-dispersive axis of the spectrometer). The BF disk extends to ~30 mrad, and an additional 5 mrad is added to further suppress dipole scattering, and all higher angles are averaged to form the off-axis signal shown in the main text. (c) The effective energy resolution of the experiment can be determined by examining the full-width at half-maximum (FWHM) of the elastic scattering peak. For the BF disk the FWHM is measured to be 13.2 meV, while in the off-axis which is more sensitive to lower energy phonons the energy resolution is reduced to 16.3 meV. 10

Figure S7. **Phonon peak shift fitting example.** (a) aADF image indicating a (green) grain and (blue) GB position chosen to show representative fits. Panel (b) show the grain fits and panel (c) shows the GB fits. 11

Figure S8. **Construction of DFT Supercell.** A model of the 10° low-angle GB is shown in (a). The dislocation-cores were constructed considering the brightness, i.e., masses of atoms, contrast in the atomic-resolution HAADF image (Figure 1(b)) and the chemistry distribution (Figure 1(e-g)), i.e., depletion of Sr and enrichment of Ti at the intracore. The orange masks in (a) highlight the alternating dislocation-cores. In the dislocation-cores region, the depleted Sr atoms were replaced by Ti atoms. Moreover, additional Ti atoms were distributed in the middle of SrO and TiO atomic planes, together with surrounding O atoms, forming rocksalt-like TiO configurations. The supercell must contain two anti-parallel GBs to satisfy periodic boundary conditions. The

distance between two anti-parallel GBs is ~ 3.9 nm. (b) Composition of large-scale atomic-resolution HAADF and DFT-optimized GB model, showing satisfactory agreement with each other. 11

Figure S9. Profile of linear combination of grain- and intra-core PPhDOS with different ratio.

From the bottom (grain) to the top (intracore), the ratio of intracore increases, resulting in the blue-shift of E1 and red-shift of E2, which is consistent with the EELS data in Figure 3(d). 12

Figure S10. Sections of DFT Charge Density at the Top Dislocation-core.

(a) Side view of the DFT supercell showing fractional coordinates of the supercell for integration. Integrated charge density from (b) 0-1 (c) 0-1/4, (d) 1/8-3/8, and (e) 1/4-1/2. Individual slices of charge density at (f) 0, (g) 1/4, (h) 3/8, and (i) 1/2. In (a-f,i) (green) Sr, (black) Ti, and (red) O atoms in the 0 plane are annotated with “+” markers while atoms in the 1/2 plane are annotated with “•” markers. Markers were excluded in (g,h) giving a cleaner unobscured image of the charge density between atomic planes. Purple annotations in (e,i) indicate rocksalt-like TiO packing. Red annotations in (h) highlight anisotropically bonded Ti and O atoms. The cyan annotation in (h) highlights a region of increased orbital overlap. The orange annotation in (i) highlights the $Ti d$ orbitals in comparison to the rocksalt $Ti d$ orbitals annotated with purple. 13

Figure S11. Sections of DFT Charge Density at the Bottom Dislocation-core.

(a) Side view of the DFT supercell showing fractional coordinates of the supercell for integration. Integrated charge density from (b) 0-1 (c) 0-1/4, (d) 1/8-3/8, and (e) 1/4-1/2. Individual slices of charge density at (f) 0, (g) 1/4, (h) 3/8, and (i) 1/2. In (a-f,i) (green) Sr, (black) Ti, and (red) O atoms in the 0 plane are annotated with “+” markers while atoms in the 1/2 plane are annotated with “•” markers. Markers were excluded in (g,h) giving a cleaner unobscured image of the charge density between atomic planes. Purple annotations in (e,i) indicate rocksalt-like TiO packing. The orange annotation in (i) highlights the $Ti d$ orbitals in comparison to the rocksalt $Ti d$ orbitals annotated with purple. 14

Figure S12. Theoretical $Ti-L_2$ spectrum comparison from Single-crystal and GB supercells.

A comparison of the $Ti-L_2$ spectrum calculated in a single-crystal $SrTiO_3$ supercell (solid orange) and in the grain of the $SrTiO_3$ grain in the GB supercell (dashed black), which is used in Figure 2. The single crystal supercell contains 135 atoms, and the large GB supercell (shown in Figure S8) contains 1130 atoms, which is not practical for high-accuracy calculations. The comparison shows that the only effect of the low-accuracy calculation is a reduction of the e_g peak intensity and an increase in the $t_{2g}-e_g$ splitting, indicating the calculation of the e_g peak is genuine and that the difference in the $t_{2g}-e_g$ splitting between the GB and bulk signals within the supercell calculations is experimentally relevant. Lastly, we note that both the changes from the high-accuracy calculation result in improved matching between the DFT calculations and the EELS data, further validating our use of the computationally feasible lower-accuracy supercell calculations in such a large supercell. A similar e_g peak intensity and $t_{2g}-e_g$ splitting correction would be expected in a higher-accuracy spectrum in the dislocation core. The theoretical EELS is Figure 2 employs the two spectra calculated at the same level of accuracy. 15

S1 Supporting Information: STEM Imaging

Images were drift-corrected using two orthogonal scan directions. An example of the drift correction for the image in **Error! Reference source not found.**(a) is shown in Figure S1. The fast-Fourier-transforms in the insets of Figure S1(a,b) are skewed due to sample drift during serial imaging. The skewness of the image is removed after drift correction, as shown by the square reciprocal lattice in the fast-Fourier-transforms in the insets of Figure S1(c).

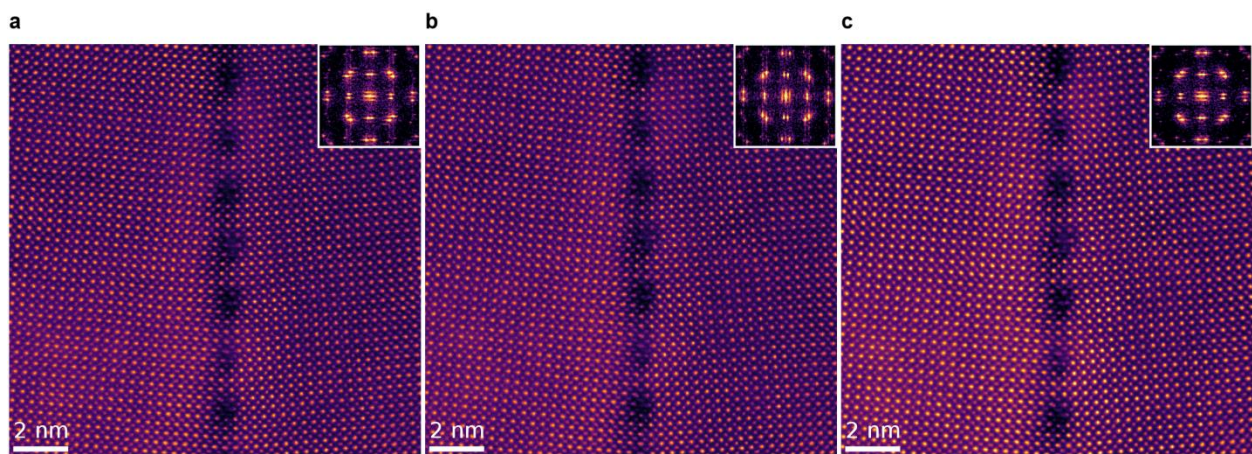


Figure S1. **Drift-correction of Aberration-corrected HAADF Image in the 10° GB.** Images acquired at (a) 0° and (b) 90° scan rotations with inset fast-Fourier-transforms showing a skewed reciprocal lattice. The image in (b) was rotated for better comparison with (a). (c) Image after drift correction.

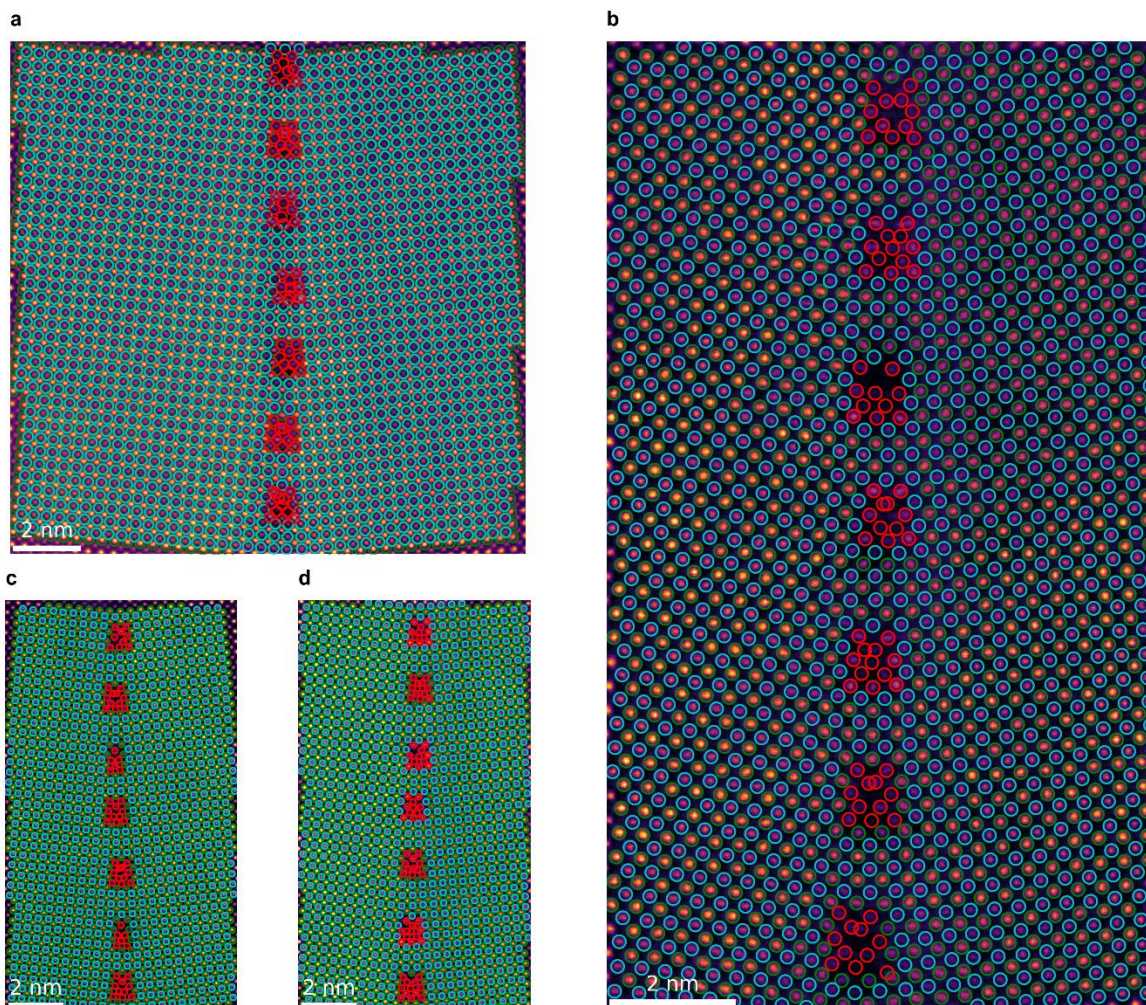


Figure S2. **Atom Positions in Four Drift-corrected HAADF Images.** (a-d) Drift-corrected HAADF images showing the (green) Sr, (cyan) Ti, and (red) core sublattices.

S2 Supporting Information: STEM Core-loss EELS

S2.1 Denoising Spectrum Images

EELS core-loss excitations have a low scattering probability. Large atomic resolution spectrum images require short dwell times to minimize the impact of sample drift and electron beam damage. The combined low scattering probability and short dwell times for core-loss spectrum images therefore results in low signal-to-noise ratios. Multivariate analysis, like singular value decomposition, provides a way to statistically denoise spectrum images by choosing a number of

statistically relevant components and removing the rest.^[1] Using discontinuities in the variance vs component number, otherwise known as a Scree plot, is a common method for identifying the number of components to include into a denoised model. However, if the spectral change(s) of interest is only present in a very small fraction of pixels or is a continuous shift over many pixels, then the spectral changes are not considered significant. In the case of GB dislocation-cores the changes in stoichiometry and structure are gradual, and the spectral shifts of the Ti- L_{23} and O- K are gradual. For example, a Scree plot for the Ti- L_{23} and O- K edge after background subtraction is shown in Figure S3. Two elbows are present in the explained variance ratio. The first elbow at component 6 includes most of the spectrum image features and will denoise the data. However, a continuous peak shift leads to a linear, slowly decaying explained variance ratio until another kink at component 110. Background, or improper background subtraction, can also lead to significant changes in the denoising process.

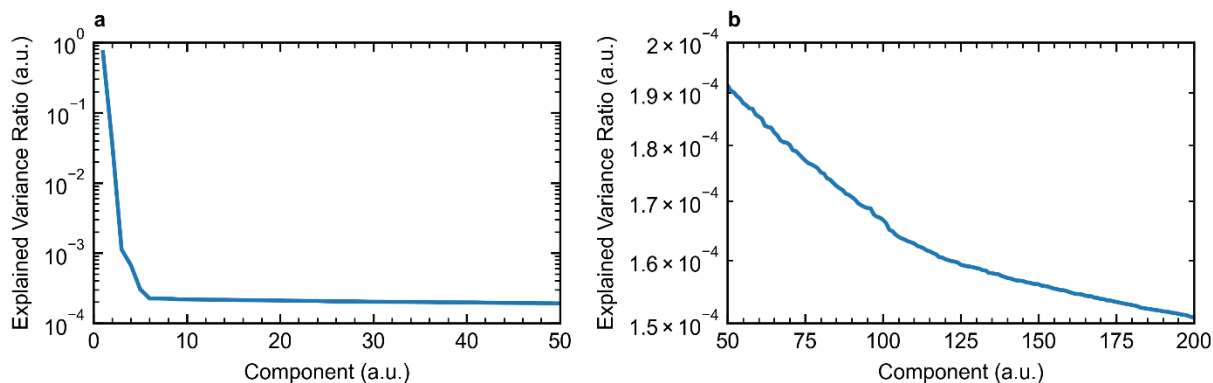


Figure S3. **SVD scree plots.** Scree plots for (a) 0-50 and (b) 50-250 components. (a) Shows the first elbow at component 4 and (b) shows the second elbow at component 110.

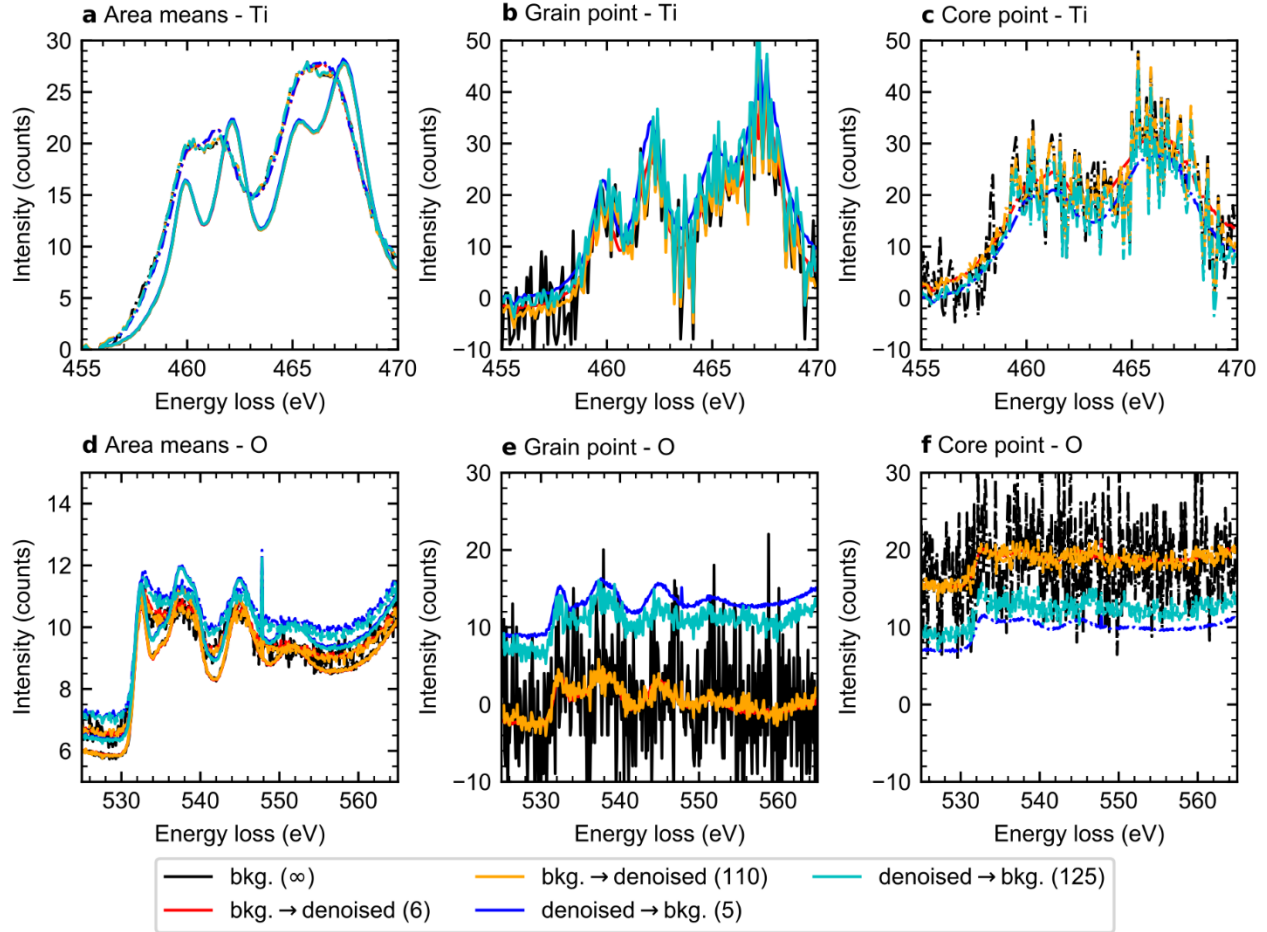


Figure S4. **SVD of TiO core-loss spectrum image of the 10° GB.** (a-c) Ti- L_{23} edge (a) averaged from each region, and from individual points in the (b) grain and (c) GB. (d-f) O- K edge (d) averaged from each region, and from individual points in the (e) grain and (f) GB. The colors of the lines correspond to the order of background subtraction and decomposition and the number of components, as indicated in the legend. In (a,c) the grain (solid) and dislocation-core (dot-dashed) signals overlap for each region because of the large number of averaged pixels.

To assure that our denoising process maintains the integrity of the original data, containing both bulk and defect spectral signatures, we plot denoised spectra constructed with multiple number of components in Figure S4, which is part of the denoising for the 10°-GB ELNES analysis in **Error! Reference source not found.** The combinations of background subtraction before and after denoising are also accessed. The area-averaged spectra from the grain and GB agree well with each other, because they contain many pixels and therefore represent a more significant

portion of the pre-denoised data. On the other hand, the data from a single point in the grain or dislocation-core are less consistent as shown in Figure S4(b,c,e,f). Firstly, more intensity is distributed between the grain ELNES peaks when more components are included. Second, background subtraction before or after denoising influences significantly the total intensity of the O-K edge. Fortunately, the size of the dislocation-cores is large enough that the difference between the grain and dislocation-cores is a significant portion of the spectrum image, so fewer components can be used and still be representative of most of the peak-shift trends while still reducing the noise. However, we note that some minor intensity redistribution is not included in the small component reconstructions here. Denoising can lead to significant oversight in other systems where peak shifts occur more abruptly over smaller fractions of a spectrum image.

S2.2 Fitting ELNES Spectrum Images

EELS from the Voronoi regions were fitted with the following steps:

1. Fit Hartree-Slater core-loss edges between ELNES and EXELFS peaks (Ranges: 450 – 481, 482 – 526, 529 – 600).
2. Fit Ti- L_{23} edges and three EXELFS Gaussians (Range: None – 450, 470 – 525). This step uses three Gaussians to approximate the EXELFS and ELNES + low-loss plural scattering.
3. Permanently freeze Ti- L_{23} core-loss edges and EXELFS and do not fit for the remainder of the fitting procedure. Fixing the Ti- L_{23} edge provides reproducible baseline for the core-loss edges based upon all post-ELNES intensity fit in step 2 and allows later for independent fitting of the ELNES intensity with minor accommodations made by the EXELFS peaks. Apart from reproducibility, removing the core-loss edges from the fit minimize fitting time and provide a more consistent procedure with the full spectrum image fit, which is explained later.

4. Fit the ELNES individually then together (Range: pre-edge – 470).
5. Freeze ELNES and unfreeze the EXELFS, then fit the EXELFS (Range: 470.5 – 525).
Adjusts the EXELFS to accounts for plural added with ELNES.
6. Unfreeze the ELNES, then fit the ELNES and EXELFS together given that both sets should be near the correct values and plural scattering accounted for (Range: 450 – 525).
7. Freeze all Ti ELNES and EXELFS Gaussians
8. Add six Gaussians for the O-*K* edge ELNES and one Gaussian for the Ti-*L*₁ edge ELNES.
Then, independently fit the O-*K* edge onset ELNES peak, Ti-*L*₁ edge ELNES peak, last O-*K* edge ELNES peak, and second to last O-*K* edge ELNES peak. Fit all O-*K* and Ti-*L*₁ edge ELNES peaks together (Range: 525 – 570).

EELS TiO SI fitting:

1. Fit core-loss edges between ELNES and EXELFS peaks
2. Fit Ti edge and EXELFS three Gaussians (Range: None – 450,470 – 525). Use the Voronoi grain EXELFS Gaussian fits as an initial condition.
3. Freeze core-loss edges and EXELFS (No more edge fits)
4. Add four ELNES Gaussians using the Voronoi grain EXELFS Gaussian fits as an initial condition. Then, fit only the ELNES Gaussians.
5. Freeze the core-loss edges and fit all ELNES and EXELFS peaks

S3 Supporting Information: STEM Vibrational EELS

While conventional STEM-EELS is limited to an energy-resolution of around 300 meV due to the cold field emission source, modern electron monochromators can improve the energy resolution to as high as 3 meV.^[2] More critically, atomic-scale spatial resolution can be achieved

alongside this energy-resolution when an off-axis geometry is used to suppress dipole scattering and enhance impact scattering.^[3-5,5-7] The combined energy and spatial resolution pave the way to correlate the vibrational properties of interfaces, grain boundary, dislocations, and other low-dimensional heterogeneities directly to the chemical and structural properties. For off-axis EELS, the beam is deflected such that the principal optic axis is no longer collected by the EELS entrance aperture. As a result, the signal collected from the annular detector no longer collects radially symmetric annular signal, resulting in the asymmetric annular darkfield image (aADF) shown in the main text.

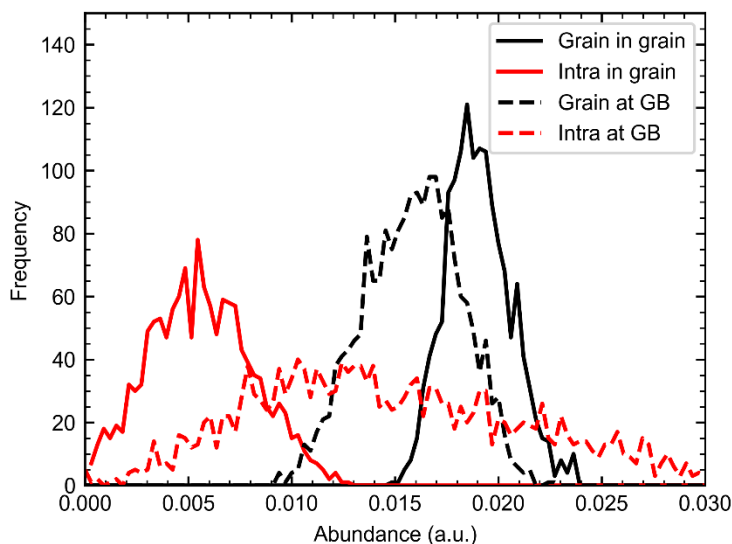


Figure S5. **NMF abundance map distributions.** Histograms of NMF abundance maps in **Error! Reference source not found.**(a,b). Distributions in the grain (solid) are from x-positions >1.5 nm from the GB center position. Distributions at the GB (dashed) are from -1.5 to 1.5 nm from the GB center position.

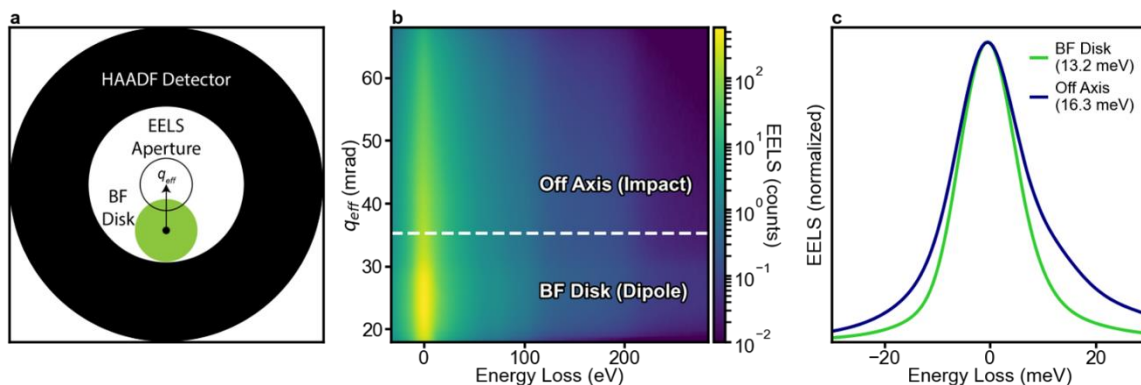


Figure S6. Off-Axis EELS Collection Geometry and Resolution. (a) Schematic for high spatial resolution vibrational EELS off-axis collection geometry. With a convergence semiangle of 30 mrad and a collection semiangle of 25 mrad, the beam is deflected by ~ 18 mrad such that the majority of the collection aperture accepts only high angle scattering events. This reduces the delocalized dipole scattering dominant in the bright field disk and emphasizes the localized impact scattering dominant at the higher angles to provide a high spatial resolution signal.^[7,8] (b) Two-dimension display of the averaged hyperspectral dataset shown for vibrational EELS in the main text. Here, the x-axis represents energy loss (the dispersive axis of the spectrometer) and the y-axis represents the effective scattering angle (the non-dispersive axis of the spectrometer). The BF disk extends to ~ 30 mrad, and an additional 5 mrad is added to further suppress dipole scattering, and all higher angles are averaged to form the off-axis signal shown in the main text. (c) The effective energy resolution of the experiment can be determined by examining the full-width at half-maximum (FWHM) of the elastic scattering peak. For the BF disk the FWHM is measured to be 13.2 meV, while in the off-axis which is more sensitive to lower energy phonons the energy resolution is reduced to 16.3 meV.

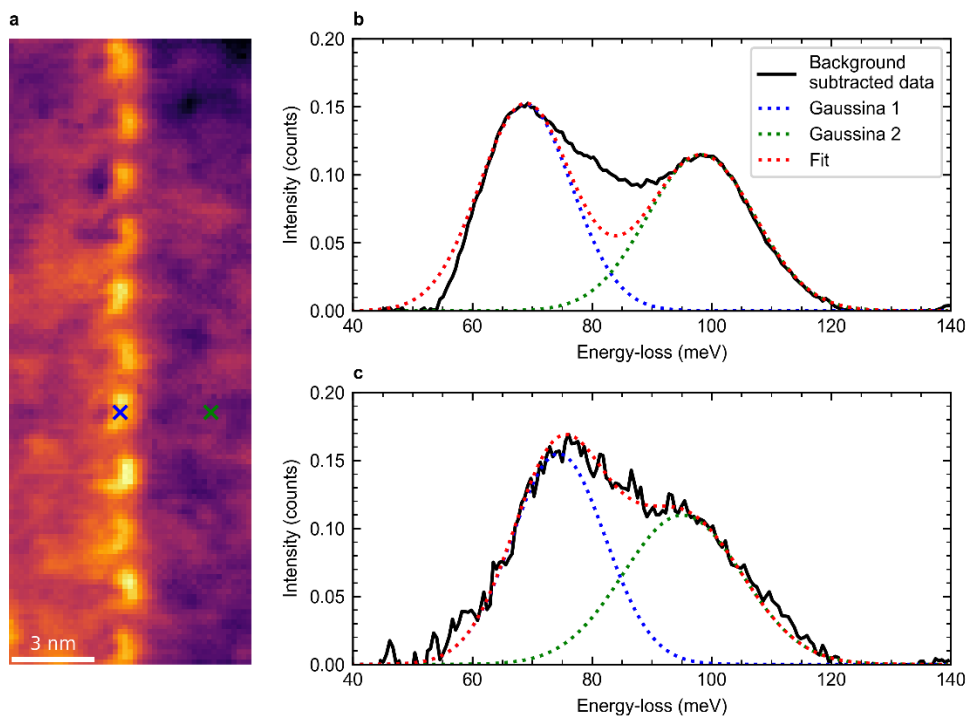


Figure S7. **Phonon peak shift fitting example.** (a) aADF image indicating a (green) grain and (blue) GB position chosen to show representative fits. Panel (b) show the grain fits and panel (c) shows the GB fits.

S4 Supporting Information: DFT

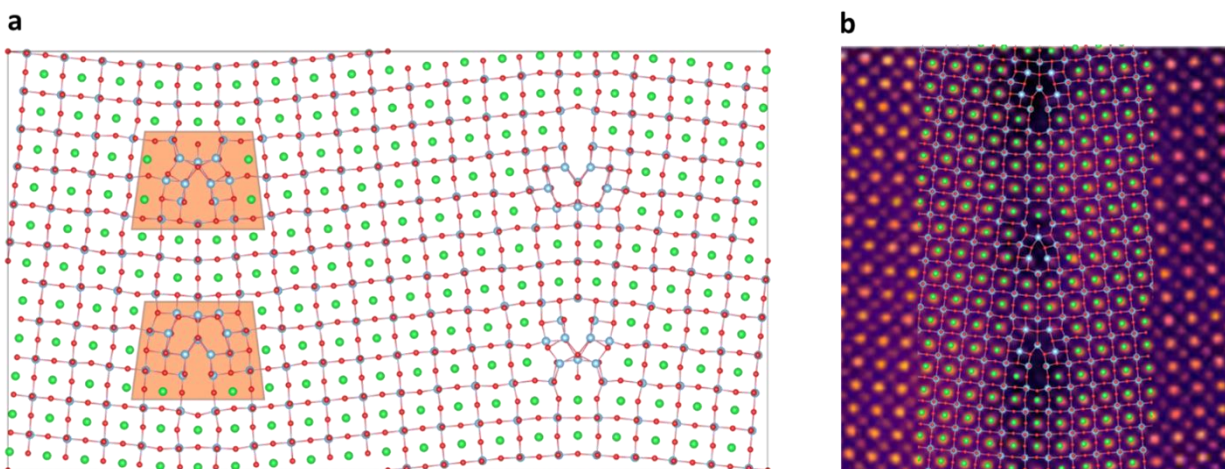


Figure S8. **Construction of DFT Supercell.** A model of the 10° low-angle GB is shown in (a). The dislocation-cores were constructed considering the brightness, i.e., masses of atoms, contrast in the atomic-resolution HAADF image (Figure 1(b)) and the chemistry distribution (Figure 1(e-g)), i.e., depletion of Sr and enrichment of Ti at the intracore. The orange masks in (a) highlight

the alternating dislocation-cores. In the dislocation-cores region, the depleted Sr atoms were replaced by Ti atoms. Moreover, additional Ti atoms were distributed in the middle of SrO and TiO atomic planes, together with surrounding O atoms, forming rocksalt-like TiO configurations. The supercell must contain two anti-parallel GBs to satisfy periodic boundary conditions. The distance between two anti-parallel GBs is ~ 3.9 nm. (b) Composition of large-scale atomic-resolution HAADF and DFT-optimized GB model, showing satisfactory agreement with each other.

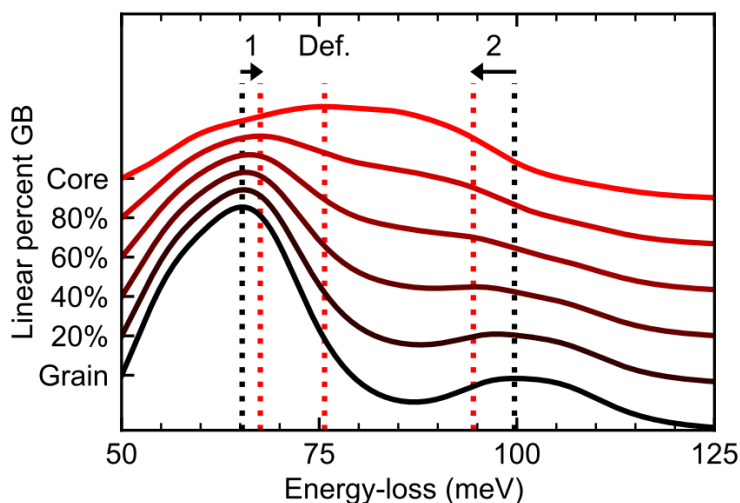


Figure S9. **Profile of linear combination of grain- and intra-core PPhDOS with different ratio.** From the bottom (grain) to the top (intracore), the ratio of intracore increases, resulting in the blue-shift of E1 and red-shift of E2, which is consistent with the EELS data in **Error! Reference source not found.**(d).

a Supercell side view

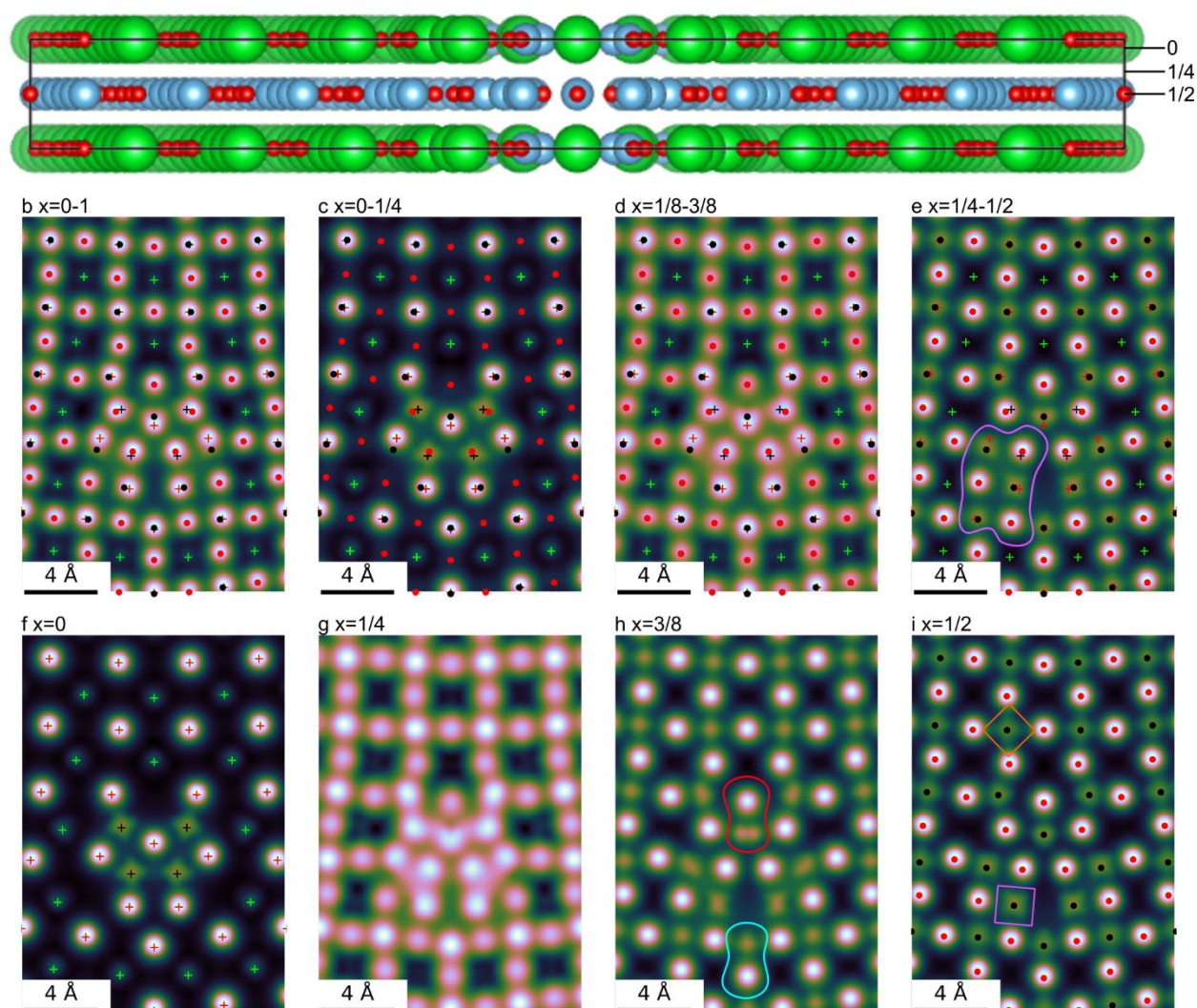


Figure S10. **Sections of DFT Charge Density at the Top Dislocation-core.** (a) Side view of the DFT supercell showing fractional coordinates of the supercell for integration. Integrated charge density from (b) 0-1 (c) 0-1/4, (d) 1/8-3/8, and (e) 1/4-1/2. Individual slices of charge density at (f) 0, (g) 1/4, (h) 3/8, and (i) 1/2. In (a-f,i) (green) Sr, (black) Ti, and (red) O atoms in the 0 plane are annotated with “+” markers while atoms in the 1/2 plane are annotated with “•” markers. Markers were excluded in (g,h) giving a cleaner unobscured image of the charge density between atomic planes. Purple annotations in (e,i) indicate rocksalt-like TiO packing. Red annotations in (h) highlight anisotropically bonded Ti and O atoms. The cyan annotation in (h) highlights a region of increased orbital overlap. The orange annotation in (i) highlights the Ti_{d} orbitals in comparison to the rocksalt Ti_{d} orbitals annotated with purple.

a Supercell side view

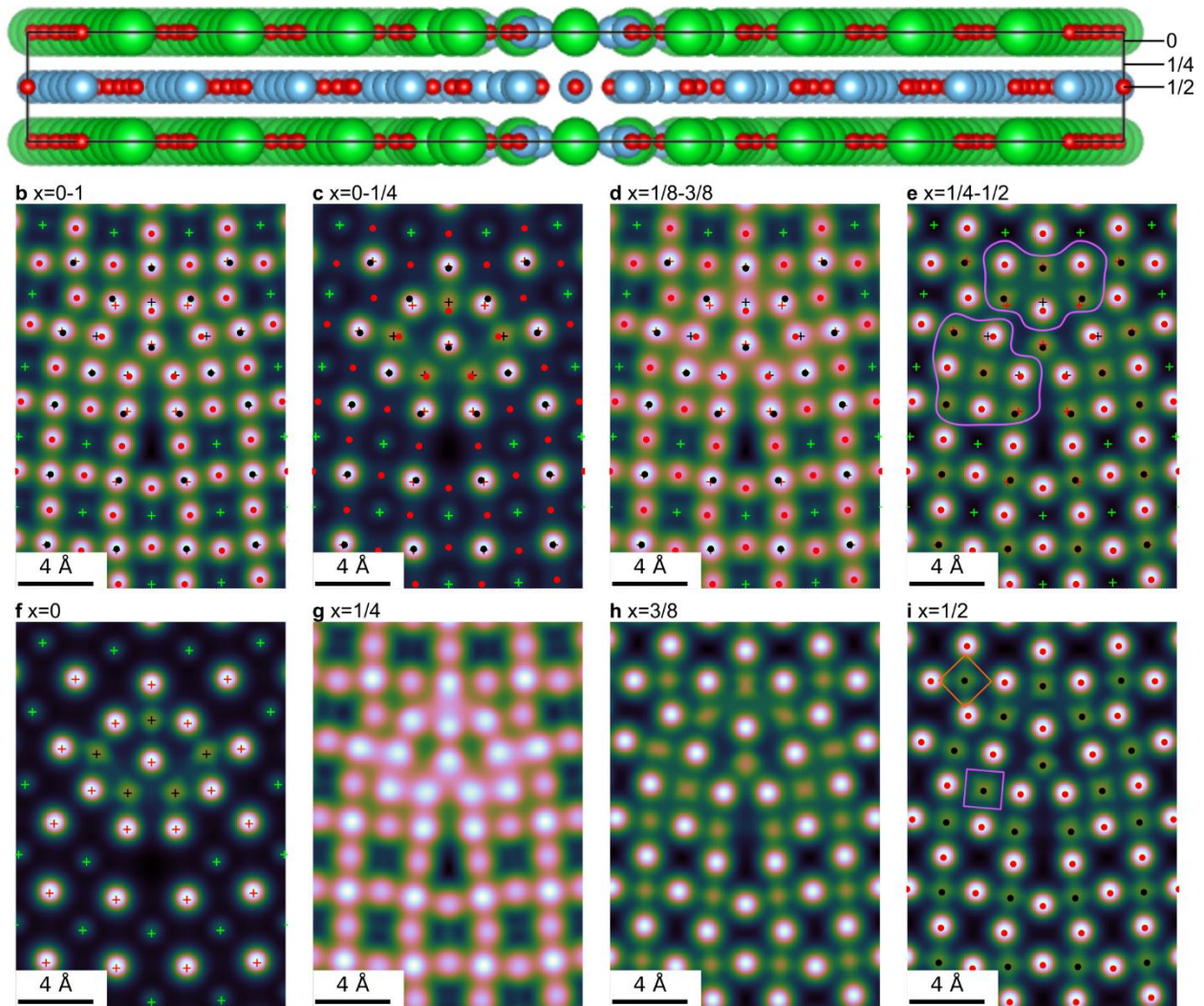


Figure S11. **Sections of DFT Charge Density at the Bottom Dislocation-core.** (a) Side view of the DFT supercell showing fractional coordinates of the supercell for integration. Integrated charge density from (b) 0-1 (c) 0-1/4, (d) 1/8-3/8, and (e) 1/4-1/2. Individual slices of charge density at (f) 0, (g) 1/4, (h) 3/8, and (i) 1/2. In (a-f,i) (green) Sr, (black) Ti, and (red) O atoms in the 0 plane are annotated with “+” markers while atoms in the 1/2 plane are annotated with “•” markers. Markers were excluded in (g,h) giving a cleaner unobscured image of the charge density between atomic planes. Purple annotations in (e,i) indicate rocksalt-like TiO packing. The orange annotation in (i) highlights the $Ti d$ orbitals in comparison to the rocksalt $Ti d$ orbitals annotated with purple.

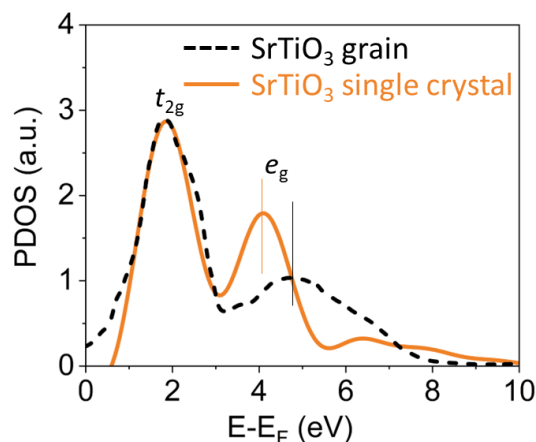


Figure S12. **Theoretical Ti- L_2 spectrum comparison from Single-crystal and GB supercells.**

A comparison of the Ti- L_2 spectrum calculated in a single-crystal SrTiO₃ supercell (solid orange) and in the grain of the SrTiO₃ grain in the GB supercell (dashed black), which is used in **Error! Reference source not found.** The single crystal supercell contains 135 atoms, and the large GB supercell (shown in Figure S8) contains 1130 atoms, which is not practical for high-accuracy calculations. The comparison shows that the only effect of the low-accuracy calculation is a reduction of the e_g peak intensity and an increase in the t_{2g} - e_g splitting, indicating the calculation of the e_g peak is genuine and that the difference in the t_{2g} - e_g splitting between the GB and bulk signals within the supercell calculations is experimentally relevant. Lastly, we note that both the changes from the high-accuracy calculation result in improved matching between the DFT calculations and the EELS data, further validating our use of the computationally feasible lower-accuracy supercell calculations in such a large supercell. A similar e_g peak intensity and t_{2g} - e_g splitting correction would be expected in a higher-accuracy spectrum in the dislocation core. The theoretical EELS is **Error! Reference source not found.** employs the two spectra calculated at the same level of accuracy.

S5 Supporting Information: References

- [1] R. F. Egerton, *Electron Energy-Loss Spectroscopy in the Electron Microscope*, Springer US, Boston, MA, **2011**.
- [2] N. Dellby, T. Lovejoy, G. Corbin, N. Johnson, R. Hayner, M. Hoffman, P. Hrncrik, B. Plotkin-Swing, D. Taylor, O. Krivanek, *Microsc. Microanal.* **2020**, *26*, 1804.
- [3] E. R. Høglund, D.-L. Bao, A. O'Hara, S. Makarem, Z. T. Piontkowski, J. R. Matson, A. K. Yadav, R. C. Haislmaier, R. Engel-Herbert, J. F. Ihlefeld, J. Ravichandran, R. Ramesh, J. D. Caldwell, T. E. Beechem, J. A. Tomko, J. A. Hachtel, S. T. Pantelides, P. E. Hopkins, J. M. Howe, *Nature* **2022**, *601*, 556.
- [4] K. Venkatraman, B. D. A. Levin, K. March, P. Rez, P. A. Crozier, *Nat. Phys.* **2019**, *15*, 1237.
- [5] F. S. Hage, G. Radtke, D. M. Kepaptsoglou, M. Lazzeri, Q. M. Ramasse, *Science* **2020**, *367*, 1124.

- [6] Z. Cheng, R. Li, X. Yan, G. Jernigan, J. Shi, M. E. Liao, N. J. Hines, C. A. Gadre, J. C. Idrobo, E. Lee, K. D. Hobart, M. S. Goorsky, X. Pan, T. Luo, S. Graham, *Nat. Commun.* **2021**, *12*, 6901.
- [7] C. Dwyer, *Physical Review B* **2014**, *89*, 054103.
- [8] J. A. Hachtel, J. R. Jokisaari, O. L. Krivanek, J. C. Idrobo, R. F. Klie, *Micros. Today* **2021**, *29*, 36.